

Du, J., Zhou, G. G., Tang, H., Turowski, J., Cui, K. F. E. (2023): Classification of Stream, Hyperconcentrated, and Debris Flow Using Dimensional Analysis and Machine Learning. - Water Resources Research, 59, 2, e2022WR033242.

<https://doi.org/10.1029/2022WR033242>

# Water Resources Research®

## RESEARCH ARTICLE

10.1029/2022WR033242

### Key Points:

- Dimensionless analyses reveal distinct transport mechanisms of debris, hyperconcentrated, and stream flows
- Boundaries drawn by Support Vector Machines distinguish different flows in the Einstein number and dimensionless flow discharge phase diagram
- Lahars exhibit a wide range of flow dynamics and sediment transport mechanisms from stream flow to debris flow

### Correspondence to:





G. G. D. Zhou,  
gordon@imde.ac.cn

### Citation:

Du, J., Zhou, G. G. D., Tang, H., Turowski, J. M., & Cui, K. F. E. (2023). Classification of stream, hyperconcentrated, and debris flow using dimensional analysis and machine learning. *Water Resources Research*, 59, e2022WR033242. <https://doi.org/10.1029/2022WR033242>

Received 14 JUL 2022  
Accepted 18 JAN 2023

## Classification of Stream, Hyperconcentrated, and Debris Flow Using Dimensional Analysis and Machine Learning

Junhan Du<sup>1,2</sup> , Gordon G. D. Zhou<sup>1,2,3</sup> , Hui Tang<sup>4</sup> , Jens M. Turowski<sup>5</sup> , and Kahlil F. E. Cui<sup>1,2</sup> 

<sup>1</sup>Key Laboratory of Mountain Hazards and Earth Surface Process, Institute of Mountain Hazards and Environment, Chinese Academy of Sciences, Chengdu, China, <sup>2</sup>University of Chinese Academy of Sciences, Beijing, China, <sup>3</sup>China-Pakistan Joint Research Center on Earth Sciences, CAS-HEC, Islamabad, Pakistan, <sup>4</sup>Section 4.7: Earth Surface Process Modelling, German Research Centre for Geosciences (GFZ), Potsdam, Germany, <sup>5</sup>Section 4.6: Geomorphology, German Research Centre for Geosciences (GFZ), Potsdam, Germany

**Abstract** Extreme rainfall events in mountainous environments usually induce significant sediment runoff or mass movements—debris flows, hyperconcentrated flows and stream flows—that pose substantial threats to human life and infrastructure. However, understanding of the sediment transport mechanisms that control these torrent processes remains incomplete due to the lack of comprehensive field data. This study uses a unique field data set to investigate the characteristics of the transport mechanisms of different channelized sediment-laden flows. Results confirm that sediments in hyperconcentrated flows and stream flows are mainly supported by viscous shear and turbulent stresses, while grain collisional stresses dominate debris-flow dynamics. Lahars, a unique sediment transport process in volcanic environments, exhibit a wide range of transport mechanisms similar to those in the three different flow types. Furthermore, the Einstein number (dimensionless sediment flux) exhibits a power-law relationship with the dimensionless flow discharge. Machine learning is then used to draw boundaries in the Einstein number-dimensionless discharge scheme to classify one flow from the other and thereby aid in developing appropriate hazard assessments for torrential processes in mountainous and volcanic environments based on measurable hydrologic and geomorphic parameters. The proposed scheme provides a universal criterion that improves existing classification methods that depend solely on the sediment concentration for quantifying the runoff-to-debris flow transition relevant to landscape evolution studies and hazard assessments.

### 1. Introduction

Steep channels make up a large portion of valley network relief in many mountain environments. Drainage area-slope scaling in steep bedrock-channel valleys departs from model predictions of fluvial bedrock incision. This has led to the suggestion that fluvial processes and debris flows are the dominant erosion processes in different parts of channel networks (McCoy, 2015; Santos & Duarte, 2006; Stock & Dietrich, 2006; Stock et al., 2005). Debris flows, hyperconcentrated flows, and stream flows are the prevalent types of sediment-laden flows in mountainous environments, each having different flow behaviors that lead to the formation of specific landforms and sedimentary structures (Costa, 1988). Fluvial sediment transport (hyperconcentrated flow and stream flow) usually happens through fluid-particle interactions characterized by rolling, saltation, or dilute suspension processes, wherein the fluid phase regulates the flow dynamics (Ancely, 2001). Hyperconcentrated flows are common in mountainous rivers (W. Li et al., 1997), where there are significant amounts of sediment from tributaries. It is typically considered as a two-phase, non-Newtonian, non-cohesive flow with separate components for the sediment and water (Costa, 1988). Stream flows usually transport bedload and suspended sediments. Large sediment particles that make up the bedload are transported via rolling, dragging, and saltation, whereas the suspended load consists of small particles traveling in the water column. Unlike stream flows and hyperconcentrated flows, the solid particles and the fluid in debris flows are completely mixed, moving together as a single cohesive, viscous-plastic body (Johnson, 1970), which vitally influences the macroscopic flow behavior (Iverson, 1997; Vallance & Iverson, 2015). Lahars are often defined as a transitional flow between hyperconcentrated flow, debris flow, and mudflow wherein the transported sediments include pyroclastic materials (Lavigne & Suwa, 2004; Pierson & Scott, 1985; Thouret et al., 2020; Vallance & Iverson, 2015).

Incorrect identification of flow types may result in severe scientific misinterpretations and inappropriate remedial practices (Costa, 1988). Different types of flows often occur as a series of channelized sediment discharges

at a point in a channel. Debris flows can block channels which can result in diversion of subsequent debris flow and hyperconcentrated flow into locations adjacent to the channel. Therefore, it is necessary to distinguish the types of flows and accurately predict when and under what conditions which type of flow may occur. However, general recognition criterion proposed in the existing literature that differentiate these flows from one another are not consistent. Various schemes have been proposed in previous literature based on the flow behavior (e.g., Middleton & Hampton, 1973), shear strength (e.g., Costa, 1988), deposition properties (e.g., Brenna et al., 2020), grain-support mechanisms (e.g., Mulder & Alexander, 2001), sediment concentration (e.g., Beverage & Culbertson, 1964) or strain rate (e.g., Jerolmack & Daniels, 2019). The sediment concentration by volume is the most common scheme applied to characterize the different flows (Dasgupta, 2003) since an increase in this quantity transforms a stream flow into a hyperconcentrated flow and eventually into a debris flow (Coussot & Meunier, 1996). The changes in sediment concentration can also strongly influence the flow rheology wherein its increase changes the flow from a Newtonian to a non-Newtonian fluid, and eventually into a viscoplastic flow (Costa, 1988). Although previous works have attempted to categorize these processes into discrete ranges of the sediment concentration spectrum (Mulder & Alexander, 2001), there is still no universally accepted scheme that distinguish one type of flow from the other. For instance, Coussot and Meunier (1996) suggested that the sediment concentrations by volume of hyperconcentrated flows should fall between 1% and 25%, while Beverage and Culbertson (1964) and Pierson et al. (1987) proposed that they should fall between 20% and 60%. Coussot and Meunier (1996) further pointed out that a single threshold is insufficient to define the entire range of flows due to differences in the dynamics and composition of the flow's front and body. Therefore, it is useful to clarify how different flow properties or variables can reflect the flow characteristics and complement our understanding of the dynamics of various processes.

This study reports and uses field observation data sets of debris flow, hyperconcentrated flow, and stream flow in channels over steep landscapes to investigate the fundamental difference between the different types of flows. Data from the literature for numerous sediment-laden flows and debris flows observed in various field sites are also analyzed. We analyze their physical properties using several dimensionless parameters. Sediment transport mechanisms and dominant stresses between different types of flows are discussed. Then, employing the machine learning method, we propose a multi-dimensional scheme to analyze various flow characteristics and improve our understanding of their sediment transport mechanisms. We examine and compare the physical thresholds and schemes for the lahars at the end.

## 2. Study Site and Data Sources

Our field site, Xiaojiang River, locates in the southwest part of China and is one of the upper reaches of the Yangtze River. The Xiaojiang River basin, with a length of 134 km and drainage area of 3,120 km<sup>2</sup>, is located in the northeastern part of Yunnan Province (N 25°2′–26°5′, E 102°2′–103°2′). The elevation of this basin ranges from 1,500 to 3,500 m and is inclined at a slope of 8° to 35° (He et al., 2003). Two strike-slip faults facilitate surface processes in this area with frequent small earthquakes (Cui et al., 2005). Along the banks of the 134-km-long trunk of Xiaojiang River, there are 140 debris-flow-dominated basins. Debris flows are most frequent in the Jiangjia Ravine (Cui et al., 1999; He et al., 2003). The Jiangjia Ravine is located in the Dongchuan Section, Yunnan (N 26°13′–26°17′, E103°06′–103°13′), close to the intersection of the Xiaojiang and Jinsha Rivers. It covers an area of about 48.6 km<sup>2</sup> with a main channel length of 13.9 km (Figure 1a). The Jiangjia Ravine is underlain by Triassic metasedimentary rocks, such as sandstone and slate, which are weak and are easily weathered into fragments, boulders, cobbles, and gravels (Zhou & Ng, 2010). There is an estimated volume of 1.23 × 10<sup>10</sup> m<sup>3</sup> of loose sediment in the Jiangjia Ravine, which becomes the primary debris flow source material (J. Chen et al., 2005). The annual rainfall in the Jiangjia Ravine ranges from 400 to 1,000 mm, 85% of which occurs during the rainy season (May–October) (Cui et al., 2005; Zhou & Ng, 2010). The high precipitation and abundant sediment source in this area induce around 12–20 debris flows annually, as measured between 1960 and 2014, making it one of the most active debris flow basins in the world (J. Chen et al., 2005). Debris flows in the Jiangjia Ravine are usually triggered by runoff generated by extreme rainfall events (>50 mm per hour) during the annual rainy seasons (Cui et al., 2005). The main channel of the Jiangjia Ravine can be divided into three sections namely, the upstream erosion section (10 km long, average slope of 17°), the middle transportation section (1.3 km and 5.1°), and the deposition section (about 4.2 km and 3.7°) close to the outlet. Debris flows in the Jiangjia Ravine are initiated from hillslopes or inside channels. Moving downslope, they erode and entrain sediments along the channel path and deposit these sediments close to the outlet or deliver them directly into the Xiaojiang River.



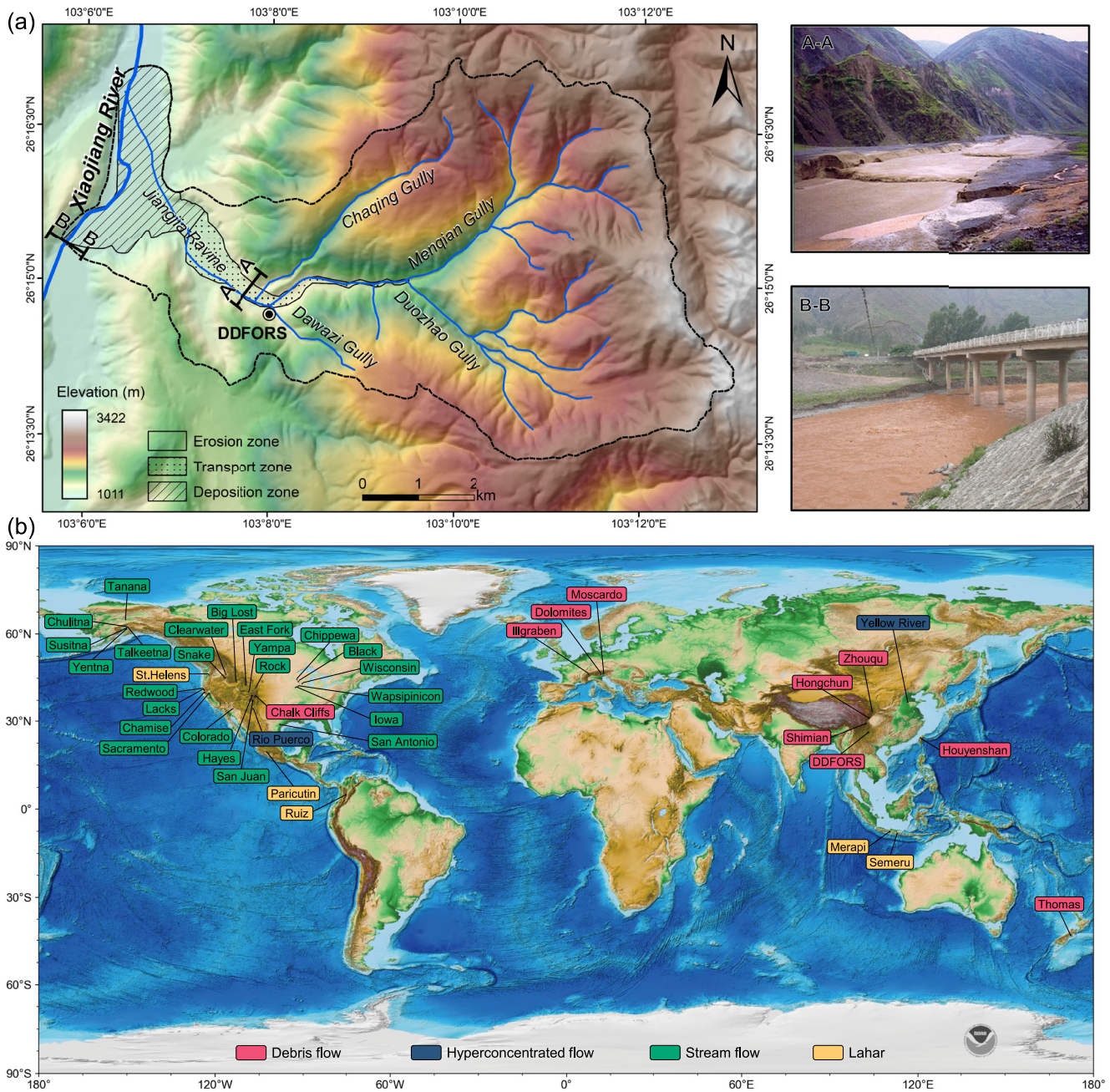


**Figure 1.** Overview of the study area. (a) Relief map of the Jiangjia Ravine. Debris-flows monitoring site in Jiangjia Ravine (A–A) and stream flows monitoring site in the Xiaojiang River (B–B); (b) Distribution of sediment-laden flows from different sites in this data set. Different color labels denotes different flow types. Base map modified from Amante and Eakins (2009).

### 2.1. Field Observations

Debris flows in the Jiangjia Ravine have been monitored since 1960 by the Dongchuan Debris Flow Observation and Research Station (DDFORS), Chinese Academy of Sciences (CAS), which is one of the longest debris flow observation sites worldwide. The measurement system consists of a steel pile foundation with strain sensors, an ultrasonic sensor, and a lead fish sampler (Hu et al., 2011; Zhou & Ng, 2010). Field measurements that are obtained in this site (Figure 1a, Section A–A) include the flow velocity ( $v$ ,  $\text{ms}^{-1}$ ), flow depth ( $h$ , m), water surface width ( $W$ , m), flow density ( $\rho_f$ ,  $\text{kg m}^{-3}$ ), and the duration of debris-flow surges ( $t$ , s) (Y. Li et al., 2015; Zhou & Ng, 2010). A typical debris flow event in the Jiangjia Ravine consists of multiple steep-front, high-viscosity,

coarse-grained surges separated by water-rich intersurge flows. The debris-flow surge front surface usually contains a large amount of coarse-grained debris accompanied by turbulent splashes. Debris flow events that do not exhibit a distinct surge front are in here referred to as continuous debris flows. For each debris flow event, the time for the surge front or flow front to pass through two monitoring cross-sections separated by a distance ( $\Delta L$ ) is recorded by a stopwatch as  $\Delta t$ . The flow velocity can then be calculated as  $v = \Delta L / \Delta t$ . The flow depth ( $h$ ) is measured continuously using an ultrasonic flow sensor (10 Hz sampling frequency) suspended 6.0 m high over the center of the channel. The density of debris flows ( $\rho_m$ ) is determined from the ratio of the mass and volume of the mixture samples taken by the sampler, which is a 61 cm high cylinder container with an 18 cm inner diameter. The sampler is initially positioned close to the channel bed and raised by hanging cables and a pulley after the flows pass. It is theoretically feasible to capture coarse grains as large as 18 cm but rare grains larger than 10 cm in practice (Hu et al., 2011). The sediment concentration  $C_s$  (by volume) is calculated as  $C_s = (\rho_m - \rho_w) / (\rho_s - \rho_w)$ , where the density of water  $\rho_w$  is 1,000 kg/m<sup>3</sup> and the density of the solid grains  $\rho_s$  is 2,650 kg/m<sup>3</sup>. This study uses 5,085 debris flow measurements (4,534 debris flow surges and 551 continuous debris flows) collected between 1960 and 2014 in the Jiangjia Ravine.

Debris flows in the Jiangjia Ravine are generally muddy, relatively shallow, rapid, and have high sediment concentrations. The dynamic properties of these events also vary significantly with time. The flow velocities range from 1 to 18 ms<sup>-1</sup>, and the flow depth and width vary between 0.15 to 4 m and 2–50 m, respectively. The average sediment concentration is 66% and the flow discharges per unit width range from 0.28 to 63.35 m<sup>2</sup>s<sup>-1</sup> with an average unit discharge of about 6.42 m<sup>2</sup>s<sup>-1</sup> for all recorded events. From field observations, it can be discerned that debris flows exhibit two modes of motion. Most debris flow events possess surges with high solid concentrations. There is also a noticeable time gap between surges for a single event. Due to grain segregation, coarse grains accumulate in debris flow fronts, making them relatively steep and dry compared to the other portions of the flow body. These coarse-grained fronts can be visually detected for each debris flow surge. The tail of the flow event is watery and is more akin to hyperconcentrated flows having low sediment concentrations. It can be said that the spatial-temporal characteristics of debris flows vary significantly between surges. On the other hand, continuous debris flows are singular persistent surges (with recorded events lasting up to 3,660 s) that have mean solid concentrations of about 47%, higher clay fractions, and longer inundation distances than debris-flow surges. The measurements and records of debris flows in Jiangjia Ravine mainly focus on the main flow body, which is the most typical representation and steady to measure.

Due to the significant amount of sediments coming from the 140 debris flow basins, such as the Jiangjia Ravine, stream flows in the Xiaojiang River have relatively higher sediment concentrations during the rainy season (He et al., 2003). To study their characteristics, we monitored flows in the Xiaojiang River at a selected section near the Xiaojiang Bridge (Figure 1a, Section B–B) during two debris flow seasons (2009 and 2010). The flow velocity is estimated by tracking the trajectory of colored plastic balls at two different locations dropped into the river over a certain reference distance. The flow depth is estimated from wet markings on a standard ruler immersed perpendicular to the flow surface for over 10 s. We also collected suspended load sediment samples to estimate sediment concentration with lead fish sampler. All sediment samples were taken from the center of the flow depth with a water-sediment mixture. This study utilizes 34 measurements from Xiaojiang Bridge, including hydrological and sediment information taken between 2009 and 2010. Field measurements show that flow velocities range from 0.9 to 2.4 ms<sup>-1</sup> with an averaged value of around 1.3 ms<sup>-1</sup>. Flow depth and width range from 0.2 to 1.1 m and 42–52 m, respectively. The flow discharges fluctuated significantly between 10 and 102 m<sup>3</sup>s<sup>-1</sup>, with an average discharge of about 40 m<sup>3</sup>s<sup>-1</sup>. Sediments in the Xiaojiang River are mainly suspended in water, and the bedload only contributes to a small portion of the transported sediments. The sediment concentration ranges from 3 to 22 kg/m<sup>3</sup> with a mean value of 10 kg/m<sup>3</sup>.

## 2.2. Data Collection

In addition to the measurements of debris flows collected in the Jiangjia Ravine and stream flows in the Xiaojiang River, we also collected additional hydrological and sediment data for hyperconcentrated flows and stream flows from the literature (Figure 1b). This compilation includes 1,035 measurements from 41 basins collected from Asia, America, Europe, and Oceania. The data set includes measurements of the grain size, discharge, river width and depth, bed slope, and morphology. For debris flows, we have included wide-range data from China (11 measurements, including Zhouqu, Hongchun Gully, Xiaojiagou, Shimian, and Houyenshan) (H. Chen



et al., 2012; Chou et al., 2013; Ni et al., 2014; C. Tang et al., 2011; Yu et al., 2010), Switzerland (9 measurements, Illgraben) (Berger et al., 2011; Wendeler et al., 2007), Italy (12 measurements include Dolomites and Moscardo) (Berti et al., 1999; Marchi et al., 2002), USA (5 measurements, Chalk Cliffs) (McCoy et al., 2012), and New Zealand (1 measurement, Mt. Thomas) (Pierson, 1980). For hyperconcentrated flows, we have included 104 measurements from the Yellow River (Gong & Jiang, 1979; Qi & Han, 1991; Qi et al., 1995, 2008) and 26 measurements from Rio Puerco (Nordin, 1963). For stream flows, we have collected 228 measurements from Yellow Rivers and 556 measurements from USA rivers (Howard, 1947; Williams & Rosgen, 1989). We have also collected data of lahars, which occur in unique geological settings and involves pyroclastic materials, from the literature on several volcanoes including Mount St. Helens, USA (Pierson, 1985; Pierson & Scott, 1985), Mt. Semeru, Indonesia (Lavigne & Suwa, 2004), Mt. Merapi, Indonesia (Lavigne & Thouret, 2003), Nevado del Ruiz, Colombia (Pierson et al., 1990), and Mt. Paricutin, Mexico (Segerstrom et al., 1956). It should be noted that the sediment-laden flows compiled here from the literature are classified based primarily on field observation and expert experience. We rely on the classification of the source publications and assume that they are accurate to our definitions.

### 3. Methods

#### 3.1. Dimensionless Numbers

To ensure that results obtained from one site are comparable to those from other sites with different geological and topographical conditions, measurements are cast into dimensionless forms (Iverson, 1997). Dimensionless numbers are useful in showing the relative importance of different sediment transport-related stresses for various systems or processes of interest (Lanzoni et al., 2017). We used 11 dimensionless parameters: dimensionless discharge ( $q_*$ ), Einstein number (dimensionless sediment flux,  $q_{s,*}$ ), Savage number ( $Sav$ ), Leighton number ( $Le$ ), Bagnold number ( $Bag$ ), mass number ( $M$ ), friction number ( $Fric$ ), Rouse number ( $Ro$ ), Stokes number ( $St$ ), Froude number ( $Fr$ ) and Reynolds number ( $Re$ ) to gain insights on flow dynamics (Ancy et al., 1999; Bagnold, 1954; Iverson, 1997; Iverson & Vallance, 2001; Munson et al., 2013; Parker, 1979; Reynolds, 1883; Rouse, 1937; Savage, 1984). All these parameters are well-defined and have been applied in previous research for both experiments and field observations (Arattano & Franzi, 2004; Badoux et al., 2009; Bennett et al., 2014; Berti et al., 1999, 2000; Chou et al., 2013; Coe et al., 2008; Marchi et al., 2002; McCoy et al., 2010, 2013; Okano et al., 2012; Suwa et al., 2009).

The general purpose of dimensional analysis is to explore the sediment transport mechanism and corresponding dominant stresses. First, from a macroscale perspective, to describe the macroscale flow behaviors (one-phase and two-phase) and general movement patterns of transported sediments (bedload and suspended load), the Stokes number and Rouse number ( $St$  vs.  $Ro$ ) are introduced. The mass number and friction number ( $M$  vs.  $Fric$ ) are employed to classify the components of the solid and fluid phases in the momentum transfer of two-phase mixtures. Furthermore, the bulk behavior is governed by the microscale processes that include grain friction (sustained contacts) and collisions, fluid viscous shear and turbulent drag and solid-fluid interactions. Correspondingly, grain frictional and collisional force, fluid viscous and turbulent force, and fluid-solid interaction forces associated with the relative fluid-grain motion jointly control the flow dynamics in two-phase mixtures. Dominant physical mechanisms reflected by the relative importance of these stresses can be evaluated through the Savage number (friction vs. collision), Bagnold number (collision vs. viscosity), Leighton number (lubrication vs. friction), and Reynolds number (turbulence vs. viscosity). We briefly introduce each dimensionless number as follows.

The dimensionless flow discharge ( $q_*$ ) is estimated from the flow discharge per unit width and the sediment grain size (Parker, 1979; Parker et al., 2007):

$$q_* = \frac{q}{\sqrt{gD^3}}, \quad (1)$$

where  $q = hv$  is the flow discharge per unit width,  $v$  is the surface flow velocity,  $h$  is the flow depth and  $g$  is the gravitational acceleration. The characteristic particle diameter  $D$  is represented by the median grain size ( $D_{50}$ ) based on the particle size distribution of sediment samples. For stream flows and hyperconcentrated flows, we used the median grain size from suspended load samples as the representative grain size. This potentially overestimates the dimensionless sediment flux due to possible underestimation of the representative grain size.

The Einstein number  $q_{s,*}$ , is a dimensionless sediment flux which is defined as:

$$q_{s,*} = \frac{q_s}{\sqrt{\frac{\rho_s - \rho_f}{\rho_f} g D^3}}, \quad (2)$$

where  $q_s$  is sediment flux per unit width from measurements,  $\rho_f$  and  $\rho_s$  are the densities of water and sediments, respectively.

The Savage number ( $Sav$ ) (Savage & Hutter, 1989) can be used to represent the ratio between the inertial and frictional stresses associated with collisions and persistent contacts among sediment grains:

$$Sav = \frac{\rho_s D^2 \dot{\gamma}^2}{\sigma_e}, \quad (3)$$

where  $\sigma_e$  represents the effective normal basal stress equal to  $\sigma - P$ ,  $\sigma$  is the normal compressive stress, and  $P$  is pore fluid pressure.  $\dot{\gamma}$  is the global shear rate, which is calculated as the ratio of the surface velocity ( $v$ ) to the flow depth ( $h$ ):

$$\dot{\gamma} = \frac{v}{h}. \quad (4)$$

We clarify that the Savage number employed here is a global parameter and represents the entire flowing layer. A similar local form, introduced as the ratio of a microscopic timescale for particle motion undergoing typical stress to a macroscopic timescale imposed by the shear rate (Ancey & Evesque, 2000; MiDi, 2004), describes the relative dominance of grain collision and friction in local contacts. Although both versions of this dimensionless number quantify the relative dominance of grain collision and friction on the flow mobility, the local version has a sounder physical interpretation and it better captures the influence of non-homogenous shear profiles (i.e., plug flows). Local flow information however is often unavailable due to difficulties in obtaining high-resolution field data. Hence, here the shear rate, the various flow parameters, and the dimensionless values derived from them are representative of the bulk flow. This convention is generally acceptable when characterizing the mobility of natural geophysical flows (Coussot & Meunier, 1996; Zhou & Ng, 2010). Based on several experimental results, it was found that collisional stresses prevail over the frictional stresses in a granular system when the Savage number exceeds 0.1 (Iverson, 1997; Savage & Hutter, 1989).

In the case of a granular-fluid mixture, the Leighton number ( $Le$ ) describes the magnitude of lubricated and frictional forces (Ancey et al., 1999; Coussot & Ancey, 1999):

$$Le = \frac{\mu_f R \dot{\gamma}}{\sigma_e \epsilon}, \quad (5)$$

where  $\mu_f$  is the viscosity of the interstitial fluid.  $R$  is the characteristic sediment radius, and  $\epsilon$  is the particle roughness which is taken as an approximate value of 10  $\mu\text{m}$ . The Leighton number can be interpreted as the ratio of the characteristic time needed for a particle to move from one point to another while immersed in a fluid and the macroscopic time controlled by the shear rate. It characterizes the transition from a frictional to a lubricated regime in granular suspensions (Coussot & Ancey, 1999). A frictional regime, where the sustained contact force becomes more predominant than lubrication and collisional forces, is obtained when the Leighton number and Savage number are both small.

The Bagnold number ( $Bag$ ) (Bagnold, 1954; Iverson, 1997) is the ratio between the inertial and viscous stresses associated with grain collisions and viscous fluid shears:

$$Bag = \frac{\lambda^{1/2} \rho_s D^2 \dot{\gamma}}{\mu_f}, \quad (6)$$

where  $\lambda$  is the linear concentration defined as  $\lambda = C_s^{1/3} / (C_{\text{max}}^{1/3} - C_s^{1/3})$ .  $C_s$  is the bulk sediment concentration, and  $C_{\text{max}}$  is the maximum sediment packing concentration. A large  $Bag$  ( $>200$ ) indicates that grain collisions dominate over viscous drag stresses (Iverson, 1997). A collisional regime ( $Sav > 0.1$  and  $Bag > 450$ ) prevails in laboratory-generated debris flows and debris flows observed in the field. The transition from frictional to collisional behavior is controlled by the viscosity of the interstitial fluid when the Bagnold number is around 1,000 (Armanini et al., 2005).

The Stokes number ( $St$ ) defines a ratio between the characteristic time in connection with the fluid flow and a characteristic time related to particle evolution (Ancey et al., 1999):

$$St = \frac{\rho_s \dot{\gamma} R^2}{\mu_f}, \quad (7)$$

The Stokes number characterizes coupling intensity between the sediment and water phases, determining whether the flow has one-phase or two-phase behaviors at the macroscale. When this ratio is small, particles are completely controlled by the fluid motion. Conversely, a large Stokes number implies that the influence of fluid drag on the motion of suspended sediments is negligible (Ancey et al., 1999; Lanzoni et al., 2017).

$Ro$  is the Rouse number that describes the ratio between the settling velocity ( $w_s$ ) and the friction velocity ( $u_*$ ) (Rouse, 1937):

$$Ro = \frac{w_s}{ku_*}, \quad (8)$$

where  $k$  is Von Karman's constant, typically taken as  $k = 0.4$ . The settling velocity ( $w_s$ ) is calculated by Dietrich's formula (Dietrich, 1982; Jiménez & Madsen, 2003):

$$\frac{w_s}{\sqrt{\frac{\rho_s - \rho_f}{\rho_f} g D}} = \left( A + \frac{B}{S_*} \right)^{-1}, \quad (9)$$

$A$  and  $B$  are experimental fitting constants, and  $S_*$  is the fluid-sediment parameter defined by Madsen and Grant (1977). The friction velocity is typically estimated as  $u^* = \sqrt{ghS}$ , where  $S$  is the channel slope. Note that the friction velocity is an approximated value for steady-state flows in which the basal shear stress is balanced by the stress component due to gravity along the streamwise direction. The Rouse number is used to characterize the dynamic balance between the upward and downward fluxes of particles in a two-phase flow. When the Rouse number is less than 2.5, the suspended load is greater than the bedload, and the sediment is transported in suspension mode while the bedload dominates over the suspension load for  $Ro > 2.5$  (Chanson, 2004).

$M$  is the mass number (Iverson & Vallance, 2001), which represents the ratio of the inertial forces of the solid component (coarse particles) and the fluid component (slurry composed of water and silt-clay) in the debris flow mixture:

$$M = \frac{C_s \rho_s}{(1 - C_s) \rho_f}. \quad (10)$$

When the mass number is greater than one, the momentum transport is dominated by solid grain dynamics indicating strong grain-to-grain processes. The mass number is strongly proportional to the sediment concentration for a given sediment source. Similarly, the friction number ( $Fric$ ) (Iverson, 1997) describes a ratio between frictional stress of the solid phase and the viscous stress of the fluid phase:

$$Fric = \frac{\lambda^{1/2} \sigma_e}{\dot{\gamma} \mu_f}. \quad (11)$$

The friction number quantifies the dominant mode of momentum transport in a two-phase flow. A large friction number suggests that frictional stresses of sediment component exceed viscous shear stresses of fluid component.

The Froude number ( $Fr$ ) defines the ratio of the flow inertia over gravity (Munson et al., 2013):

$$Fr = \frac{v}{\sqrt{gh}}. \quad (12)$$

The Froude number reflects the wave-making resistance of free-surface flows. Flows can be distinguished into subcritical ( $Fr < 1$ ), critical ( $Fr = 1$ ), and supercritical flows ( $Fr > 1$ ). When the fluid inertia becomes more predominant than the viscous effect, it gives a rise to the turbulent flow. And the Reynolds number ( $Re$ ) describes the magnitude of fluid turbulence:

$$Re = \frac{\rho_f v h}{\mu_f}. \quad (13)$$



The Reynolds number reflects the fluid inertia and it is typically used to characterize flow patterns (laminar or turbulent flows). An open-channel flow is considered to be laminar when  $Re \leq 10$ , fully turbulent when  $Re \geq 500$ , and an intermediate regime exists between these limiting values.

### 3.2. Support Vector Machine (SVM) and Confusion Matrix

A machine learning model, the Support Vector (SV) algorithm, is employed in this study. The Support Vector (SV) algorithm is a class of nonlinear search algorithms based on a statistical learning theory developed by Vapnik (Smola & Schölkopf, 2004; Vapnik, 1964). Support vector algorithms, including Support Vector Machine (SVM), have been developed as classification tools and widely applied in different data science problems. We employ an open-source SVM library-LIBSVM developed by Chang and Lin (2011) to evaluate our data set. SVM is a supervised learning system in which sample classification is determined by finding a hyperplane that produces the optimal separation between different classes. The hyperplane is constructed from the SVM training set points (support vectors), differentiating it from other separating approaches. When two classes are not linearly separable, a kernel function maps the data into a higher-dimensional space so that a linear hyperplane can separate the classes. For our data set, we define the kernel function as a log function that maps data into the log-log space. The best hyperplane for a support vector machine is the one with the most significant margin between the two classes:

$$y = \text{sgn}(q_*) = \text{sgn}\left(\sum_{i=1}^n w_i s_i + b\right) = \text{sgn}(ws + b), \quad (14)$$

in which  $y$  represents the class label (i.e., debris flows, hyperconcentrated flows, and stream flows),  $s$  is the feature variable,  $w$  and  $b$  are the hyperplane parameters, and  $\text{sgn}$  denotes the sign function. The boundaries are designed to find  $s$  and  $b$  that minimize  $|w|$ . All data points are represented by  $(s_j, y_j)$  while the support vectors are  $(s_j, q_*)$  on the boundary. It has been proven that a maximum-margin classifier has the best generalization capabilities on unseen data compared to other possible separating hyperplane solutions (Cortes & Vapnik, 1995).

This study applies the support vector machine with a kernel function to determine the boundary that characterizes debris flows from hyperconcentrated flow and stream flow. The SVM method is more suitable for dealing with two-class classifications than other more complicated approaches, which are more appropriate for data having multiple classes. We only use a support vector machine to determine the hyperplane rather than a classifier. The boundaries obtained from SVM separate debris-flow events from fluvial events. Since SVM only takes the data points close to the boundary to drive the hyperplane, it compensates for our limited data set for both hyperconcentrated flow and stream flow.

We used a confusion matrix (error matrix) to analyze and define thresholds objectively. The confusion matrix is a specific table that assesses classification model performance. It has been widely applied for rainfall intensity-duration thresholds (Fawcett, 2006; Raymond et al., 2020; Staley et al., 2013; Swets, 1988). This table generally identifies four possible outcomes of a binary classifier model: true-positive (TP), false-positive (FP), true-negative (TN), and false-negative (FN). A true-positive is recorded for any threshold between flow types when a quantity exceeds the measured threshold, indicating a correct classification. In the same way, true-negative results are when the data points are correctly predicted to be below the boundary and therefore fall under another classification. False negatives and false positives are erroneous predictions. A good classifier model should maximize the number of TP predictions and minimize FP and FN predictions (Fawcett, 2006; Swets, 1988). The overall classifier performance is quantified as either true positive rate ( $TP_{rate}$ , recall rate or sensitivity), false positive rate ( $FP_{rate}$ , fall-out rate), false negative rate ( $FN_{rate}$ , miss rate) and true negative rate ( $TN_{rate}$ , specificity) which are calculated as:

$$TP_{rate} = \frac{TP}{TP + FN} \quad (15)$$

$$FP_{rate} = \frac{FP}{FP + TN} \quad (16)$$

$$TN_{rate} = \frac{TN}{FP + TN} \quad (17)$$

$$FN_{rate} = \frac{FN}{TP + FN} \quad (18)$$

It should be noted that the data for SVM classification models are usually separated into training and validation data sets. Since our purpose in this study is to draw the threshold objectively, we will use all data points from our study site and literature for testing thresholds. We also calculated the threat score ( $TS$  critical success index) and  $F_1$  score, which are also widely applied to depict the predictive capability of classification models (Visa et al., 2011):

$$TS = \frac{TP}{TP + FN + FP} \quad (19)$$

$$F1 = \frac{2TP}{2TP + FP + FN} \quad (20)$$

The threat score is a measure of the overall classifier model performance. For a perfect model, the threat score would equal one, in which each incorrect prediction (false-negative or false-positive event) reduces the value of the threat score (Raymond et al., 2020; Schaefer, 1990). We chose the threat score as a metric in the optimization analysis because it equally weights the reduction in the score for both false-negative and false-positive events. The  $F1$  score measures the accuracy of a binary classification model and is a harmonic mean of the precision and recall.  $F1$  gets the highest possible value (one) when it indicates perfect precision and recall, and  $F1$  receives the lowest value (zero) if either the precision or the recall is zero. We will use these metrics to evaluate both boundaries between debris flows, hyperconcentrated flows, and stream flows.

## 4. Results

### 4.1. Dimensionless Characterization

We used different combinations of dimensionless parameters as evaluated in Section 3.1 to gain insight into the multi-stress mechanisms and their role in sediment transport of the different types of flows. Sediment particle behavior is studied in Figure 2a by plotting the Rouse number  $Ro$  against the Stokes number  $St$ . It is observed that sediments are mostly suspended in a fluid ( $Ro < 1$ ), and the suspended load is greater than the bedload for representative grain sizes of various sediment-laden flows. For some debris flows in Illgraben, Chalk Cliffs, Houyenshan, Zhouqu, Hongchun, Xiaojiagou, and Jiangjia Ravine,  $St > 1$ , indicating a negligible fluid drag effect (Ancy et al., 1999; Lanzoni et al., 2017). Hyperconcentrated flows and stream flows are largely similar in that Stokes numbers do not exceed 0.1 and can be extremely small (down to  $10^{-6}$ ). Debris flows and lahars, and fluvial flows (hyperconcentrated flows and stream flows) collapse into two distinct power-law trends in the  $Ro$ - $St$  scheme. The mass number  $M$  and friction number  $Fric$  are plotted against each other to study the momentum transfer between the solid and fluid phases (Figure 2b). Debris flows usually have larger mass numbers, mostly exceeding the threshold value ( $M = 1$ ), compared to hyperconcentrated flows and stream flows. When  $M$  is greater than one, solid inertial stresses exceed that of the fluid in a two-phase flow (Iverson & Vallance, 2001). Correspondingly, the ratio of the momentum transfer between frictional contact among grains and viscous shear of fluid, characterized by  $Fric$ , exhibits a positive relationship with mass number. Debris flow falls into a different trend from other flow types in the  $Fric$ - $M$  space.

The Leighton number  $Lei$  and Savage number  $Sav$  exhibit consistent variation as both reflect the transition from a frictional regime to a higher shear state. A smaller Leighton number and Savage number indicate that grain friction prevails in a granular suspension (Ancy et al., 1999). In the  $Lei$ - $Sav$  phase diagram, debris flows, lahars, and hyperconcentrated flows follow one varying trend while stream flows are separated. This is because both Savage number and Leighton number were designed for characterizing the concentrated granular suspensions (Ancy et al., 1999; Savage, 1984), while dilute suspensions, like stream flows, are not comparable to concentrated suspensions. For instance, the smaller Leighton number of stream flows compared to debris flow does not mean that the endured grain contacts in debris flows are less than that in stream flows. The reduced  $Sav$  may also be because the viscous effect in stream flows is weaker than that in debris flow, leading to a smaller ratio value. Therefore, the relative magnitude of fluid lubrication and grain collision to grain friction reflected by the Leighton number and Savage number is still valid for a certain flow type. We combined Bagnold number  $Bag$  and Savage number  $Sav$ , given the various classifications of rheological regimes proposed in terms of these two numbers

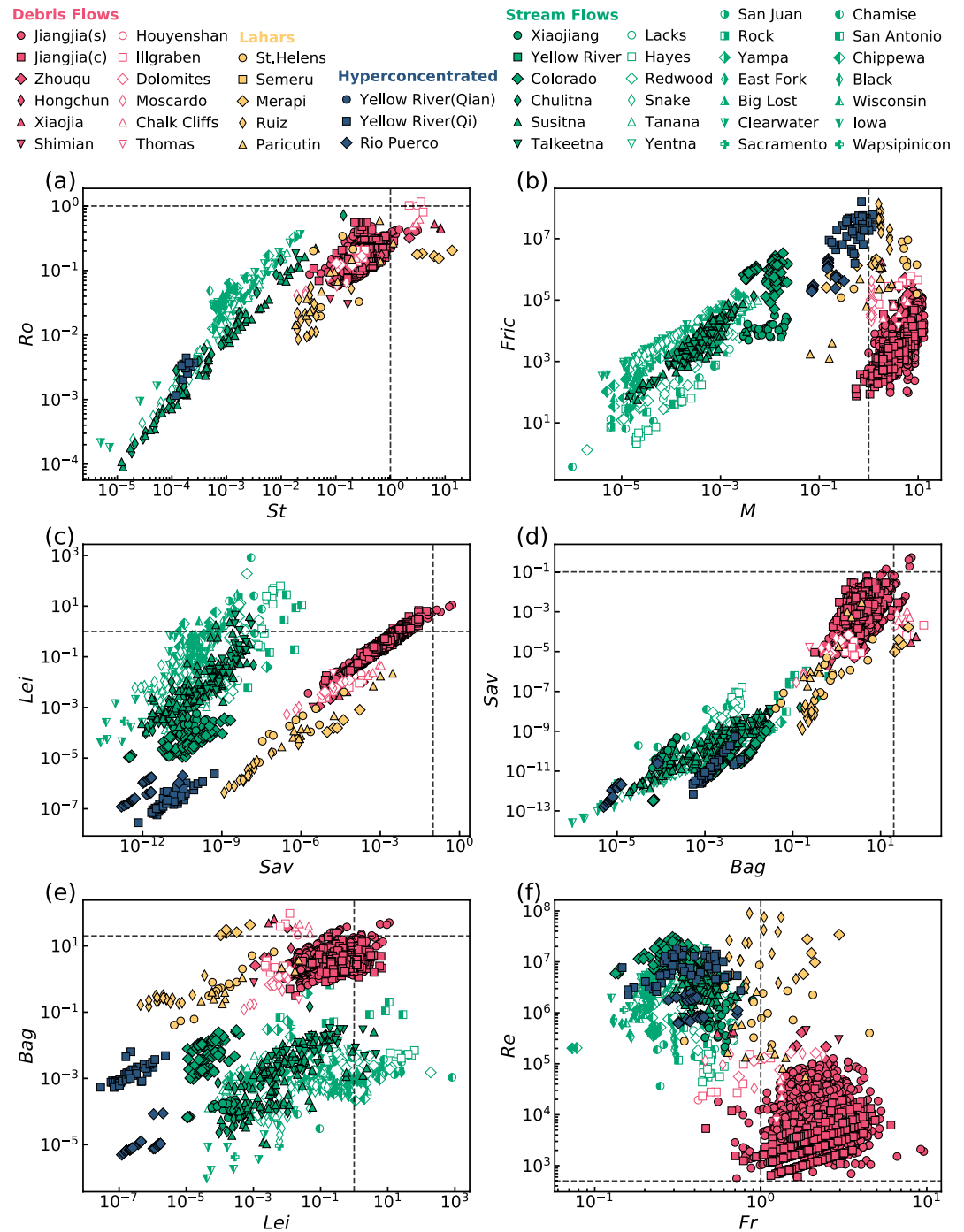


**Figure 2.** Field measurements of debris flows (red), hyperconcentrated flows (blue), and stream flows (green) in different field sites are plotted in the (a) ( $Ro$ ,  $St$ ), (b) ( $M$ ,  $Fric$ ), (c) ( $Sav$ ,  $Lei$ ), (d) ( $Sav$ ,  $Bag$ ), (e) ( $Lei$ ,  $Bag$ ), (f) ( $Fr$ ,  $Re$ ) parameter space. Data of flowing lahars are also plotted as yellow symbols. Dashed lines denote the transition limits of the different rheological regimes derived from literature.

(Figure 2d) (Armanini et al., 2005; Takahashi & Das, 2014). A distinct gap between fluvial sediment-laden flows and debris flows can be observed in the  $Sav - Bag$  phase diagrams (Figure 2d). Debris flows usually have a greater Bagnold number and Savage number than hyperconcentrated flow and stream flow, suggesting that intense grain collisions prevail in debris flow as it typically contains a large number of coarse particles (boulders and cobbles). Small  $Bag$  in hyperconcentrated flows and stream flows indicates that grain collisional

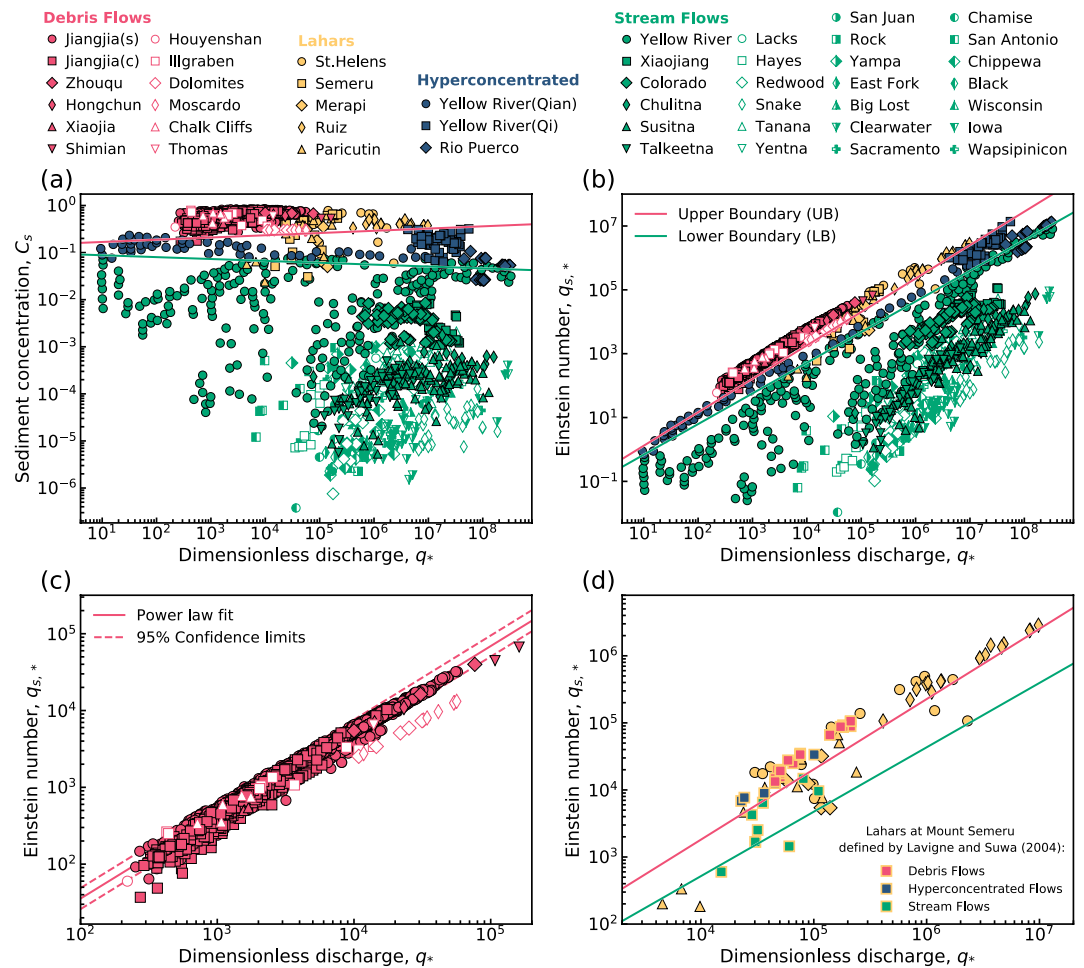


**Figure 3.** (a) Sediment concentration and dimensionless discharge for the different study sites considered. (b) Einstein number  $q_{s,*}$  versus the dimensionless sediment flux  $q_s$ . The boundaries are derived from Support Vector Machine (SVM) machine learning model. (c) Einstein number for debris flows as a function of dimensionless discharge. The red solid line represents a power-law fit while the dashed lines represent 95% confidence limits. (d) Application of the proposed boundaries on the data set for lahars in Mount Semeru (Lavigne & Suwa, 2004).

stress is negligible while viscous drag predominates in fluvial sediment-laden flow. In addition, Figure 2e plots the Bagnold number  $Bag$  against the Leighton number  $Lei$  since they both account for the hydrodynamic effect of viscous fluid (Ancey et al., 1999). A larger Leighton number and smaller Bagnold number indicate that the lubricated contacts and viscous drag are stronger than grain frictional and collisional contacts, respectively. In Figure 2f, Reynolds number  $Re$ , which describes the fluid inertial effect, is plotted against the Froude number  $Fr$ . Debris flow has smaller Reynolds number than fluvial flows since the slurry with high viscosity extremely damps the fluid turbulence. Stream flow and hyperconcentrated flow are subcritical flows having Froude number smaller than one while debris flows mostly belong to the supercritical flow ( $Fr > 1$ ). It shows that  $Re$  in hyperconcentrated flow and stream flow is greater than in debris flows, suggesting that role of fluid turbulence is non-negligible in fluvial sediment transport. Hyperconcentrated flow behaves similarly to stream flows as both have largely overlap in distribution, while debris flow locates in the opposite zone with fluvial sediment-laden flows in the  $Re$ - $Fr$  scheme (Figure 2f).

#### 4.2. Upper and Lower Boundaries

Sediment-laden flows span an exceedingly wide range of dimensionless discharges  $q_*$ , from  $10^1$  to  $10^9$  (Figure 3a). The sediment concentration in stream flows can vary significantly for a given flow discharge. In contrast,  $C_s$  of hyperconcentrated flows and debris flows converge into a specific range. Debris flows contain a higher sediment



concentration than stream flows for the same discharge. However, an ambiguous zone is observed wherein data points corresponding to the three types of flows overlap. The sediment concentration for hyperconcentrated flows in the Yellow River and Rio Puerco and debris flows from the Dolomites, Moscardo, and Jiangjia Ravine overlap over the range  $0.1 < C_s < 0.4$ .

In Figure 3b, the dimensionless discharge corresponding to the different flow types is plotted against the Einstein number  $q_{s,*}$  (dimensionless sediment flux). Debris flows cover a relatively narrow range of  $q_*$  from  $10^2$  to  $10^5$ . Relative to debris flows, the fluvial sediment-laden flows (stream flow and hyperconcentrated flow) cover a wider range of  $q_*$  from  $10^1$  to  $10^9$ . We used the SVM to draw boundaries separating data points of debris flows (red), hyperconcentrated flows (blue), and stream flows (green) in the dimensionless discharge and Einstein number. The SVM implements the boundaries and data points close to the edge to define a new set of critical discharge functions by maximizing the utility function of the confusion matrix. The SVM implements the boundaries and data points close to the edge to define a new set of critical discharge functions by maximizing the utility function of the confusion matrix. An upper boundary (UB) defines the threshold between debris flows and hyperconcentrated flows, and a lower boundary (LB) separates hyperconcentrated flow from stream flow. Both upper boundary and lower boundary exhibit power-law trends that can be formally defined as:

$$q_{s,*} = cq_*^d, \quad (21)$$

where  $q_{s,*}$  is the Einstein number,  $q_*$  is the dimensionless flow discharge. By employing the SVM, dimensionless coefficients  $c$  and  $d$  of the upper and lower boundaries are obtained, respectively. The best classification results for the upper boundary and the lower boundary yield:

$$UB : q_{s,*} = 0.12q_*^{1.05}, \quad (22)$$

and

$$LB : q_{s,*} = 0.07q_*^{0.96}. \quad (23)$$

Upper and lower boundaries divide the  $q_*$ - $q_{s,*}$  parameter space into three regions, each corresponding to a different type of flow (Figure 3b). Equations 22 and 23 can be re-written in terms of the sediment concentration ( $C_s$ ) as:

$$C_{s,u} = 0.15q_*^{0.05}, \quad (24)$$

and

$$C_{s,l} = 0.1q_*^{-0.04}, \quad (25)$$

where  $C_{s,u}$  and  $C_{s,l}$  are the sediment concentration thresholds for the upper boundary separating debris flows and hyperconcentrated flows and the lower boundary between hyperconcentrated flows and stream flows, respectively.

Confusion matrix analysis is performed on upper and lower boundaries. The discharge thresholds in H. Tang et al. (2019b) were from numerical simulations of runoff-generated debris flows and floods in the post-fire setting as triggering thresholds. In contrast, our objective thresholds are determined from direct field observations using the methods described in the previous section. We identified the best predictions of debris flow and hyperconcentrated flow occurrences with a power-law kernel function for different analyzed boundaries. This result is consistent with direct observations of the power-law boundaries separating the three types of flows. Confusion matrix analysis of upper boundary yields 5,120 true-positive events, 123 true-negative events, and only three false-negative events. Analysis of lower boundary yields 119 true-positive events, 800 true-negative events, and 18 false-positive events. In addition, we also find that  $q_{s,*}$  of debris flows vary with the  $q_*$  as a power-law, similar to that of the two boundaries:

$$q_{s,*} = 0.23q_*^{1.1}. \quad (26)$$

The solid line is the best fit, while dashed lines represent the 95% confidence limits for our data set (Figure 3c).

### 4.3. Flow Characteristics of Lahars

Lahar is a special flow type since it occurs in volcanic regions and contains large amounts of pyroclastic materials. Sediment concentrations in lahars vary greatly, ranging from 2% to 70%, hereby resulting in diverse flow

dynamics. The majority of lahar events are similar to debris flows in most dimensional parameter phase diagrams, in that both have relatively high Rouse and Stokes numbers (Figure 2a), Mass and friction numbers (Figure 2b), Savage and Bagnold numbers (Figure 2d). However, lahars are also distributed in areas more akin to hyperconcentrated flow and stream flow in the  $M - Fric$  scheme (Figure 2b). Lahars in this data set can be both supercritical and subcritical flows (Figure 2f). In general, lahars are typically located in a transition zone between debris flows and fluvial sediment-laden flow. From the schemes of *Sav*, *Lei*, and *Bag*, it can be seen that lahars exactly fill the gap between debris flows and fluvial sediment-laden flows where lahars have minimal overlap with debris flows and hyperconcentrated flows (Figures 2c–2e). The dominant stress mechanisms and corresponding flow regimes of lahar span a quite wide range as the composition and hydrologic conditions vary greatly.

In Figure 3d, the  $q_*$  and  $q_{s,*}$  of 83 lahar events are plotted along with upper boundary (red) and lower boundary (green). The  $q_*$  range from  $10^3$  to  $10^7$  and  $q_{s,*}$  varies between  $10^2$  and  $10^7$ . Lavigne and Suwa (2004) reported lahars (35 events) in Mt. Semeru that occurred between 1999 and 2000 and classified them as debris flows, hyperconcentrated flows, and stream flows based on field observation. These three types of flows classified by Lavigne and Suwa (2004) are independent of the data set that we used to train the SVM. Therefore, these classifications can be used for the validation of the boundaries obtained from SVM. The  $q_*$  and  $q_{s,*}$  values of Mt. Semeru lahars are depicted as filled squares wherein debris flow-like lahars are red (20 events), hyperconcentrated lahar flows are blue (5 events), and stream flow-like lahars (10 events) are green. Data points of the debris flow locate above UB, corresponding to true-positive predictions. Five hyperconcentrated flows locate very close to or alongside upper boundary making their classification according to our framework ambiguous. All 10 stream flow events from field observation are close to or above the lower boundary and better fit the classification as hyperconcentrated flows. Lahars that happened in Nevado del Ruiz and most of the events in Mt. St. Helens can be considered to be debris flows, while the majority of lahars in Mt. Merapi are hyperconcentrated flows. Based on our  $q_{s,*} - q_*$  scheme, lahars in Paricutin show substantial variability between stream flow to debris flow (Figure 3d).

## 5. Discussion

### 5.1. Flow Dynamics and Sediment Transport Mechanisms

Many particle-scale processes (grain collisions, grain enduring contacts, viscous and turbulent fluid shear, and solid-fluid interactions) determine the overall rheological behavior of the mixture and, consequently, its flow dynamics and sediment transport mechanisms. However, due to the dramatic temporal and spatial variation in flow characteristics of a single flow event, these complex processes are usually impossible to monitor and measure in large scales. In this regard, dimensional analysis allows us to derive reasonable representations of the flow dynamics. Regardless of their scale, events with similar dimensionless parameters are said to be dynamically similar. Examination of dimensionless parameters allows for the evaluation of particle-scale effects and understanding of sediment transport mechanisms without the difficulty of reproducing differently generated stresses associated with reduced geometrical scales. The difference in dominant stress regimes in debris flows, hyperconcentrated flows, and stream flows leads to different sediment transport mechanisms and damage processes to infrastructure. For stream flow and hyperconcentrated flow, sediment is primarily supported and transported by the shear traction of the fluid phase, as indicated in Figure 2. Therefore, these two types of flows can be treated as fluid-dominated flows. On the contrary, for debris flows, dispersive pressure associated with grain collisions plays a vital role in sediment transport (Figures 2c–2e). The silt, clay, and water make up the slurry mixture, contributing to the ability to transport sediments resulting from the fluid density. The matrix structure can provide cohesive strength for the suspension of coarse particles in debris flows, generating a high sediment load. Therefore, sediment transport in debris flows is less fluid-dependent (Mulder & Alexander, 2001). Determination of the primary grain-support mechanisms can also help provide criterion for different hazard scenarios for lahars based only on measurable hydrologic properties, as demonstrated in Figure 3d.

The sediment transport capacity of a given flow has been an established concept across a wide range of domains in different landscapes (fluvial, aeolian, coastal, hillslope, debris flow, and glacier) (Wainwright et al., 2015). Both the sediment supply (i.e., supply limited rivers) and flow dynamics (i.e., transport-limited rivers) jointly control the transport capacity of open-channel flows (Gilbert, 1877, 1914). The previous works usually assume an unlimited sediment supply and an equilibrium concentration (Gilbert, 1877, 1914; Wainwright et al., 2015). However, based on hydraulic and sediment transport data of various sediment-laden flows, we found that fluvial transport, such as stream flows and hyperconcentrated flows, strongly depends on the flow discharge. Sediment

**Table 1**  
Confusion Matrix for Upper Boundary Between Debris Flow and Hyperconcentrated Flow

	Debris flow	Hyperconcentrated flow
Positive	5,120 (TP)	7 (FP)
Negative	3 (FN)	123 (TN)

Note. TP (True Positive): above threshold, Debris flow observed; FP (False Positive): above threshold, Hyperconcentrated flow observed; FN (False Negative): below threshold, Debris flow observed; TN (True Negative): below threshold, Hyperconcentrated flow observed.

flux and concentration increase with the flow discharge for a wide range of field sites. In contrast, debris flows tend to exert their sediment transport capacity in equilibrium (Figures 3a and 3b).

### 5.2. Physical Thresholds

Results here demonstrate that the dimensionless flow discharge and sediment flux (expressed as the Einstein number) are generally related to phase changes observed between debris flows, hyperconcentrated flows, and stream flows (Figure 3b). The previously suggested sediment concentration criterion strongly depends on the sediment source and may not directly reflect the sediment transport mechanisms, because it does not express dependence on dynamic flow properties. It is unclear how changes in sediment concentra-

tion will directly result in changes in rheology and sediment transport mechanisms since that will depend on the amount of eroded sediment and the resulting changes in the flow dynamics in the water column following entrainment. As a consequence, criterion based entirely on the sediment concentration may lead to misinterpretations of the sediment transport mechanisms required to guide hazard mitigation strategies and structural countermeasures within a given basin. Compared to the single sediment concentration criterion used in previous research, the dimensionless flow discharge-Einstein number scheme can capture more hydrologic information and reflect the sediment transport mechanism more effectively.

The upper and lower boundaries in the  $q_*-q_{s,*}$  parameter space that define the thresholds separating one type of flow from the other are drawn using the Support Vector Machines method. The  $TP_{rate}$ ,  $FP_{rate}$ ,  $TN_{rate}$ , and  $FN_{rate}$ , derived from both the upper boundary and the lower boundary, are presented in Tables 1–3 to summarize the model performance. Quantitative analysis of these predictions by Confusion Matrix yielded encouraging results (Table 3): the upper boundary is found to have extreme  $TP_{rate}$  (0.999) and low  $FP_{rate}$  (0.053), while the lower boundary has a high  $TP_{rate}$  (0.915) and a lower  $FP_{rate}$  (0.022). The TS and F1 scores for both boundaries are 0.998 and 0.999, 0.804 and 0.891, indicating that UB, between debris flows and hyperconcentrated flows, is better than lower boundary in separating hyperconcentrated flows and stream flows. This implies that debris flows, based only on their  $q_*$  and  $q_{s,*}$  values, are distinct from the two other flows considered here, whereas the difference between hyperconcentrated and stream flows remains ambiguous. The relative weakness of lower boundary is probably due to the underestimation of the sediment flux in stream flows which may result from ignoring the sediment from bedload transport. However, applying the lower boundary threshold in conjunction with runoff-only simulations will potentially compensate for these underestimations (H. Tang et al., 2019a, 2019b). For hazard management, it is first necessary to assess the target disaster type, and then take corresponding mitigation strategies to avoid, prevent, or control it. For instance, a slit dam should be built for debris flows and a closed dam for water floods. Since one ravine can have different types of mountain hazards, it is important to classify the dominant hazard type and strengthen the mitigation strategy according to the dominant flow type. Although field monitoring systems can measure fundamental hydrologic information like flow depth, and flow velocity, a quantitative framework that is able to analyze the basic measurements and further classify the flow type is necessary. Therefore, the proposed classification framework of this study provides a quantitative reference scheme for engineers. Using the classification scheme, engineers can analyze historical measurements and determine the main flow type of the target area, thus making appropriate hazard mitigation strategies.

Our predictions support the transition among different sediment-laden flows and further emphasize the need to understand the physical processes that lead to the transition from infiltration-excess runoff to debris flows in mountainous environments. Despite the relative efficiency of the upper boundary in classifying debris flows, their dimensionless flow discharge and sediment flux partly overlap with those of fluvial flows. Field observations and temporal averaging may not be sufficient to capture the hydrologic conditions necessary to distinguish the different flows from one another. Numerous measurements in data set may distract the focus of the distinction of the overlap zone between different flow types. The support vector machines fundamentally

**Table 2**  
Confusion Matrix for Lower Boundary Between Hyperconcentrated Flow and Stream Flow

	Hyperconcentrated flow	Stream flow
Positive	119 (TP)	18 (FP)
Negative	11 (FN)	800 (TN)

Note. TP (True Positive): above threshold, Hyperconcentrated flow observed; FP (False Positive): above threshold, Stream flow observed; FN (False Negative): below threshold, Hyperconcentrated flow observed; TN (True Negative): below threshold, Stream flow observed.

**Table 3**  
Evaluation Metrics for Upper and Lower Boundaries

	$TP_{rate}$	$FP_{rate}$	$FN_{rate}$	$TN_{rate}$	$TS$ score	$F_1$ score
Upper Boundary	0.999	0.053	0.946	0.0005	0.998	0.999
Lower Boundary	0.915	0.022	0.978	0.084	0.804	0.891

Note.  $TP_{rate}$ : True Positive rate;  $FP_{rate}$ : False Positive rate;  $FN_{rate}$ : False Negative rate;  $TN_{rate}$ : True Negative rate;  $TS$ : Threat Score;  $F_1$ : F1 score; see text in Section 3.2 for definitions.

avoid the influence of the data set we used on the boundaries because support vectors will be drawn before determining the boundaries, emphasizing the weight of data near the transition between flow types. Therefore, the boundaries for these three types of flow in our proposed dimensional scheme drawn by support vector machines appear reasonable and statistically sound.

In many natural flow events, three phases of flow exist simultaneously over a reach of a channel and pass a given point in the channel sequentially. In this regard, the classification frameworks based on geomorphological and sedimentological features of flow deposits provide another perspective that helps infer the hydrodynamic characteristics of past flows and to inform hazard models of likely characteristics of future flows (Brenna et al., 2020;

Keaton, 2019). The deposits of these different sediment-laden flows have distinctive sedimentary structures: stream flow deposits are stratified, graded, and fining upward; hyperconcentrated flow deposits are fully clast supported; debris-flow deposits are unsorted, unstratified, and fully matrix-supported (Keaton, 2019). The inclination of the imbricated clasts tends to increase significantly with the transition from stream flow to hyperconcentrated flow and debris flow deposition (Brenna et al., 2020). In addition to the deposition structure, the composition of different flow deposits varies significantly. Debris flows typically contains numerous megaclasts, if these are available in the source area (Anderson et al., 1984; Keaton, 2019). Flow type can affect organic matter content in the fine fraction of sediment deposits left by debris flows tend to be moderately higher than that of stream flow deposits (Brenna et al., 2020).

### 5.3. New Interpretation of Lahars and Debris Floods

While the absolute values of the upper boundary and lower boundary thresholds derived here are specific to non-volcanic environments, the framework employed here is general and potentially applicable to lahars (Figure 3d). Jerolmack and Daniels (2019) considered lahars as debris flows that include pyroclastic materials released during volcanic eruptions. In that context, lahars usually have high sediment concentrations (0.4–0.6) and a wide range of dimensionless strain rates ( $10^{-5}$  to  $10^{-1}$ ). The term lahar is general and does not consider particular flow dynamics and physical properties. Therefore, an additional benefit of establishing the Einstein number-discharge threshold framework is that, unlike traditional lahar hazard assessments, this framework is based on the hydrologic properties of a lahar. For example, this framework can be used to study the hydraulic properties of volcanic material. Following an eruption, hydraulic roughness, rainfall interception, and vegetation will change over time, consequently influencing the runoff generation and lahar flow process. Furthermore, given data constraining how sediment source and hydrologic properties change as a function of time since the eruption, the thresholds derived here for dimensionless discharge and the Einstein number can be applied to inform mitigation strategies for lahar-related hazards.

Previous literature has mentioned or studied debris floods as a different type of extreme flow (e.g., Brenna et al., 2020; Church & Jakob, 2020; Wilford et al., 2004), but we propose to consider it as a nonspecific term that includes a flow event that has all phases of sediment discharge and probably includes tree branches. Data points corresponding to debris floods are not used to draw the boundaries in the  $q^*-q_{s,*}$  space. First, insufficient reliable data encode the hydrodynamics and sediment transport mechanisms of debris floods due to the difficulty in collecting them. In this regard, interpreting flow depositions based on the geological features can provide an ancillary perspective to access the debris floods. Second, rainfall-generated floods or debris floods are usually very large-scale hazards compared to debris flows and occur in catchments with large drainage areas. The hydrodynamic thresholds developed here are consistent with previously published flood research (Figure 3). However, the proposed framework for generating thresholds based on hydrodynamic criterion is a promising alternative method for distinguishing and assessing the potential of different extreme flows in the future.

## 6. Conclusions

This work aims to interpret the flow dynamics and sediment transport mechanism across different sediment-laden flows, and propose a criterion for classifying debris flows, hyperconcentrated flows, and stream flows from one another. To this end, an extensive data set is collected for these geophysical flows obtained from detailed field



observations and literature surveys. The collected data includes measurements of the dynamic properties of individual flow events from different parts of the world. The Support vector machines (SVM) and confusion matrices are used to draw the boundaries that distinguish the different flow types.

Several dimensional numbers are used to shed light on predominant flow regimes and prevailing stresses that control the sediment transport of the different flow types. Sediment movement modes and overall momentum transfer pattern in fluvial processes (stream flows and hyperconcentrated flows) are more fluid-dominated wherein the turbulent and viscous stresses associated with the fluid phase prevails. On the other hand, the solid phase, relevant to the grain frictional and collisional stresses, plays a more predominant role in the dynamics of debris flows.

Distinction between flow types is most evident when data points are projected in the dimensionless discharge-Einstein number parameter space. This shows that the flow discharge and the sediment flux are major factors that make debris flows, hyperconcentrated flows, and stream flows different from each other. Applying SVM on the flow data in this parameter space yields two power-law boundaries—debris flows locate above the upper boundary, stream flows are below the lower boundary, while hyperconcentrated flows are sandwiched in between. The classification drawn by the SVM boundaries is further applied to lahar flows wherein it is found that these volcanic flows exhibit a wide range of flow behaviors akin to stream flows and debris flows.

The classification framework proposed here is based on hydrodynamic conditions and sediment availability. It improves existing classification framework that depends solely on sediment concentration and deposit morphology. These thresholds can be used to address different mass flow hazards and landscape evolution within steep basins. However, some ambiguity still exists in the classification of hyperconcentrated flows and stream flows which may be improved through more reliable hydrologic and sediment data.

## Notation

$v$	Flow velocity [ $LT^{-1}$ ]
$h$	Flow depth [ $L$ ]
$Q$	Flow discharge [ $L^3T^{-1}$ ]
$q$	Flow discharge per unit width [ $L^2T^{-1}$ ]
$q_s$	Sediment flux per unit width [ $L^2T^{-1}$ ]
$q_*$	Dimensionless flow discharge per unit width
$q_{s,*}$	Dimensionless sediment flux per unit width or Einstein number
$g$	Gravity acceleration rate [ $LT^{-2}$ ]
$W$	Water surface width [ $L$ ]
$C_s$	Sediment concentration
$D_{50}$	Median size of sediment [ $L$ ]
$\dot{\gamma}$	Shear rate [ $T^{-1}$ ]
$\rho_f$	Flow density [ $ML^{-3}$ ]
$\rho$	Density of water [ $ML^{-3}$ ]
$\rho_s$	Density of sediment [ $ML^{-3}$ ]
$\mu_f$	Viscosity of the fluid [ $ML^{-1}T^{-1}$ ]
$St$	Stokes number
$Ro$	Rouse number
$M$	Mass number
$Fric$	Friction number
$Sav$	Savage number
$Lei$	Leighton number
$Bagn$	Bagnold number
$Fr$	Froude number
$Re$	Reynolds number
$e$	Particle roughness [ $L$ ]
$w_s$	settling velocity [ $LT^{-1}$ ]
$u_*$	Friction velocity [ $LT^{-1}$ ]
$\Delta L$	Distance between two monitoring stations [ $L$ ]

$\Delta t$	Time difference [T]
$S$	Channel slope
$\sigma_e$	Effective normal basal stress [ $ML^{-1}T^{-2}$ ]
$\sigma$	Normal compressive stress [ $ML^{-1}T^{-2}$ ]
$P$	Pore fluid pressure [ $ML^{-1}T^{-2}$ ]
$\lambda$	Linear concentration
$C_{\max}$	Closet packing sediment concentration
$y$	Class label
$s$	Feature variable
$w, b$	Hyperplane parameters
$\text{sgn}$	Sign function
$s_j, y_j$	Data points
$(s_j, q_s)$	Data point on the boundary
$TP_{\text{rate}}$	True positive rate, recall rate or sensitivity
$FP_{\text{rate}}$	False positive rate or fall-out rate
$FN_{\text{rate}}$	False negative rate or miss rate
$TN_{\text{rate}}$	True negative rate or specificity
$TS$	Threat score or critical success index
$C_{s,u}$	Sediment concentration thresholds for upper boundary
$C_{s,l}$	Sediment concentration thresholds for lower boundary
$c, d$	Power-law function parameters

## Data Availability Statement

The authors note all of the data in the present work are available through the following link: <https://doi.org/10.5281/zenodo.7371277>.

## Acknowledgments

The authors would like to thank the Editor Hamid Moradkhani, the Associate Editor Christophe Ancely, the reviewer Jeffrey R. Keaton and other anonymous reviewers whose comments and suggestions greatly improved this work. The authors also thank the Dongchuan Debris Flow Observation and Research Station, Chinese Academy of Sciences for providing the field measurements. The authors appreciate Prof. Qiang Zou and Prof. Jinshan Zhang for their contribution to Figure 1a. The authors acknowledge financial support from the International Science & Technology Cooperation Program of China (No. 2018YFE0100100), Key Collaborative Research Program of the Alliance of International Science Organizations (Grant ANSO-CR-KP-2021-07), CAS "Light of West China" Program, and Sino-German Mobility Program (No. M-0145).

## References

- Amante, C., & Eakins, B. (2009). *ETOPO1 global relief model converted to PanMap layer format* (Vol. 10). NOAA-National Geophysical Data Center, PANGAEA. <https://doi.org/10.1594/PANGAEA.769615>
- Ancely, C. (2001). Debris flows and related phenomena. In *Geomorphological fluid mechanics* (pp. 528–547). Springer.
- Ancely, C., Coussot, P., & Evesque, P. (1999). A theoretical framework for granular suspensions in a steady simple shear flow. *Journal of Rheology*, 43(6), 1673–1699. <https://doi.org/10.1122/1.551067>
- Ancely, C., & Evesque, P. (2000). Frictional-collisional regime for granular suspension flows down an inclined channel. *Physical Review E*, 62(6), 8349–8360. <https://doi.org/10.1103/PhysRevE.62.8349>
- Anderson, L. R., Keaton, J. R., Saarinen, T. F., & Wells, W. G. (1984). *The Utah landslides, debris flows, and floods of May and June 1983*. National Academy Press.
- Arattano, M., & Franzl, L. (2004). Analysis of different water-sediment flow processes in a mountain torrent. *Natural Hazards and Earth System Sciences*, 4(5/6), 783–791. <https://doi.org/10.5194/nhess-4-783-2004>
- Armanini, A., Capart, H., Fraccarollo, L., & Larcher, M. (2005). Rheological stratification in experimental free-surface flows of granular-liquid mixtures. *Journal of Fluid Mechanics*, 532(4), 269–319. <https://doi.org/10.5194/nhess-4-783-2004>
- Badoux, A., Graf, C., Rhyner, J., Kuntner, R., & McArdell, B. W. (2009). A debris-flow alarm system for the Alpine Illgraben catchment: Design and performance. *Natural Hazards*, 49(3), 517–539. <https://doi.org/10.1007/s11069-008-9303-x>
- Bagnold, R. A. (1954). Experiments on a gravity-free dispersion of large solid spheres in a Newtonian fluid under shear. *Proceedings of the Royal Society of London. Series A. Mathematical and Physical Sciences*, 225(1160), 49–63. <https://doi.org/10.1098/rspa.1954.0186>
- Bennett, G., Molnar, P., McArdell, B., & Burlando, P. (2014). A probabilistic sediment cascade model of sediment transfer in the Illgraben. *Water Resources Research*, 50(2), 1225–1244. <https://doi.org/10.1002/2013WR013806>
- Berger, C., McArdell, B. W., & Schlunegger, F. (2011). Sediment transfer patterns at the Illgraben catchment, Switzerland: Implications for the time scales of debris flow activities. *Geomorphology*, 125(3), 421–432. <https://doi.org/10.1016/j.geomorph.2010.10.019>
- Berti, M., Genevois, R., LaHusen, R., Simoni, A., & Tecca, P. (2000). Debris flow monitoring in the Acquabona watershed on the Dolomites (Italian Alps). *Physics and Chemistry of the Earth - Part B: Hydrology, Oceans and Atmosphere*, 25(9), 707–715. [https://doi.org/10.1016/S1464-1909\(00\)00090-3](https://doi.org/10.1016/S1464-1909(00)00090-3)
- Berti, M., Genevois, R., Simoni, A., & Tecca, P. R. (1999). Field observations of a debris flow event in the Dolomites. *Geomorphology*, 29(3–4), 265–274. [https://doi.org/10.1016/S0169-555X\(99\)00018-5](https://doi.org/10.1016/S0169-555X(99)00018-5)
- Beverage, J. P., & Culbertson, J. K. (1964). Hyperconcentrations of suspended sediment. *Journal of the Hydraulics Division*, 90(6), 117–128. <https://doi.org/10.1061/jycejaj.0001128>
- Brenna, A., Surian, N., Ghinassi, M., & Marchi, L. (2020). Sediment–water flows in mountain streams: Recognition and classification based on field evidence. *Geomorphology*, 371, 107413. <https://doi.org/10.1016/j.geomorph.2020.107413>
- Chang, C.-C., & Lin, C.-J. (2011). LIBSVM: A library for support vector machines. *ACM Transactions on Intelligent Systems and Technology*, 2(3), 1–27. <https://doi.org/10.1145/1961189.1961199>
- Chanson, H. (2004). *Hydraulics of open channel flow*. Elsevier.

- Chen, H., Zhang, L., Chang, D., & Zhang, S. (2012). Mechanisms and runout characteristics of the rainfall-triggered debris flow in Xiaojiagou in Sichuan Province, China. *Natural Hazards*, 62(3), 1037–1057. <https://doi.org/10.1007/s11069-012-0133-5>
- Chen, J., He, Y., & Wei, F. (2005). Debris flow erosion and deposition in Jiangjia Gully, Yunnan, China. *Environmental Earth Sciences*, 48(6), 771–777. <https://doi.org/10.1007/s00254-005-0017-z>
- Chou, H.-T., Chang, Y.-L., & Zhang, S.-C. (2013). Acoustic signals and geophone response of rainfall-induced debris flows. *Journal of the Chinese Institute of Engineers*, 36(3), 335–347. <https://doi.org/10.1080/02533839.2012.730269>
- Church, M., & Jakob, M. (2020). What is a debris flood? *Water Resources Research*, 56(8), e2020WR027144. <https://doi.org/10.1029/2020WR027144>
- Coe, J. A., Kinner, D. A., & Godt, J. W. (2008). Initiation conditions for debris flows generated by runoff at Chalk Cliffs, central Colorado. *Geomorphology*, 96(3), 270–297. <https://doi.org/10.1016/j.geomorph.2007.03.017>
- Cortes, C., & Vapnik, V. (1995). Support-vector networks. *Machine Learning*, 20(3), 273–297. <https://doi.org/10.1023/A:1022627411411>
- Costa, J. E. (1988). Rheologic, geomorphic and sedimentologic differentiation of water floods, hyperconcentrated flows and debris flows. *Flood Geomorphology*, 113–122.
- Coussot, P., & Ancey, C. (1999). Rheophysical classification of concentrated suspensions and granular pastes. *Physical Review E*, 59(4), 4445–4457. <https://doi.org/10.1103/PhysRevE.59.4445>
- Coussot, P., & Meunier, M. (1996). Recognition, classification and mechanical description of debris flows. *Earth-Science Reviews*, 40(3–4), 209–227. [https://doi.org/10.1016/0012-8252\(95\)00065-8](https://doi.org/10.1016/0012-8252(95)00065-8)
- Cui, P., Chen, X., Waqng, Y., Hu, K., & Li, Y. (2005). Jiangjia Ravine debris flows in south-western China. In *Debris-flow hazards and related phenomena* (pp. 565–594). Springer.
- Cui, P., Wei, F., & Li, Y. (1999). Sediment transported by debris flow to the lower Jinsha River. *International Journal of Sediment Research*, 14(4), 67–71.
- Dasgupta, P. (2003). Sediment gravity flow-the conceptual problems. *Earth-Science Reviews*, 62(3–4), 265–281. [https://doi.org/10.1016/S0012-8252\(02\)00160-5](https://doi.org/10.1016/S0012-8252(02)00160-5)
- Dietrich, W. E. (1982). Settling velocity of natural particles. *Water Resources Research*, 18(6), 1615–1626. <https://doi.org/10.1029/JC087iC12.p09489>
- Fawcett, T. (2006). An introduction to ROC analysis. *Pattern Recognition Letters*, 27(8), 861–874. <https://doi.org/10.1016/j.patrec.2005.10.010>
- Gilbert, G. K. (1877). *Report on the geology of the Henry Mountains*. US Government Printing Office.
- Gilbert, G. K. (1914). *The transportation of debris by running water* (Vol. 86). US Government Printing Office.
- Gong, S., & Jiang, D. (1979). Soil erosion and its control in small watersheds of the loess plateau. *Scientia Sinica*, 12(11), 1302–1313.
- He, Y., Xie, H., Cui, P., Wei, F., Zhong, D., & Gardner, J. (2003). Gis-based hazard mapping and zonation of debris flows in Xiaojiang Basin, southwestern China. *Environmental Geology*, 45(2), 286–293. <https://doi.org/10.1007/s00254-003-0884-0>
- Howard, C. S. (1947). *Suspended sediment in the Colorado River, 1925–41*. US Government Printing Office.
- Hu, K., Wei, F., & Li, Y. (2011). Real-time measurement and preliminary analysis of debris-flow impact force at Jiangjia Ravine, China. *Earth Surface Processes and Landforms*, 36(9), 1268–1278. <https://doi.org/10.1002/esp.2155>
- Iverson, R. M. (1997). The physics of debris flows. *Reviews of Geophysics*, 35(3), 245–296. <https://doi.org/10.1029/97RG00426>
- Iverson, R. M., & Vallance, J. W. (2001). New views of granular mass flows. *Geology*, 29(2), 115–118. [https://doi.org/10.1130/0091-7613\(2001\)029\(0115:NVOGMF\)2.0.CO;2](https://doi.org/10.1130/0091-7613(2001)029(0115:NVOGMF)2.0.CO;2)
- Jerolmack, D. J., & Daniels, K. E. (2019). Viewing Earth's surface as a soft-matter landscape. *Nature Reviews Physics*, 1(12), 1–15. <https://doi.org/10.1038/s42254-019-0111-x>
- Jiménez, J. A., & Madsen, O. S. (2003). A simple formula to estimate settling velocity of natural sediments. *Journal of Waterway, Port, Coastal, and Ocean Engineering*, 129(2), 70–78. [https://doi.org/10.1061/\(ASCE\)0733-950X\(2003\)129:2\(70\)](https://doi.org/10.1061/(ASCE)0733-950X(2003)129:2(70))
- Johnson, A. M. (1970). *Physical processes in geology: A method for interpretation of natural phenomena; intrusions in igneous rocks, fractures, and folds, flow of debris and ice*. Freeman.
- Keaton, J. R. (2019). *Review of contemporary terminology for damaging surficial processes: Stream flow, hyperconcentrated sediment flow, debris flow, mud flow, mud flood, mudslide*. Association of Environmental and Engineering Geologists. Retrieved from <https://repository.mines.edu/handle/11124/173147>
- Lanzoni, S., Gregoretti, C., & Stancanelli, L. (2017). Coarse-grained debris flow dynamics on erodible beds. *Journal of Geophysical Research: Earth Surface*, 122(3), 592–614. <https://doi.org/10.1002/2016JF004046>
- Lavigne, F., & Suwa, H. (2004). Contrasts between debris flows, hyperconcentrated flows and stream flows at a channel of Mount Semeru, East Java, Indonesia. *Geomorphology*, 61(1–2), 41–58. <https://doi.org/10.1016/j.geomorph.2003.11.005>
- Lavigne, F., & Thouret, J.-C. (2003). Sediment transportation and deposition by rain-triggered lahars at Merapi Volcano, Central Java, Indonesia. *Geomorphology*, 49(1–2), 45–69. [https://doi.org/10.1016/S0169-555X\(02\)00160-5](https://doi.org/10.1016/S0169-555X(02)00160-5)
- Li, W., Qi, P., & Sun, Z. (1997). Deformation of river bed and the characteristics of sediment transport during hyper-concentrated flood in the Yellow River. *International Journal of Sediment Research*, 12(3), 72–79.
- Li, Y., Liu, J., Su, F., Xie, J., & Wang, B. (2015). Relationship between grain composition and debris flow characteristics: A case study of the Jiangjia Gully in China. *Landslides*, 12(1), 19–28. <https://doi.org/10.1007/s10346-014-0475-z>
- Madsen, O. S., & Grant, W. D. (1977). Quantitative description of sediment transport by waves. *Coastal Engineering*, 1976(15), 1092–1112. <https://doi.org/10.9753/icce.v15.64>
- Marchi, L., Arattano, M., & Deganutti, A. M. (2002). Ten years of debris-flow monitoring in the Moscardo Torrent (Italian Alps). *Geomorphology*, 46(1–2), 1–17. [https://doi.org/10.1016/S0169-555X\(01\)00162-3](https://doi.org/10.1016/S0169-555X(01)00162-3)
- McCoy, S. W. (2015). Research focus: Infrequent, large-magnitude debris flows are important agents of landscape change. *Geology*, 43(5), 463–464. <https://doi.org/10.1130/focus052015.1>
- McCoy, S. W., Kean, J. W., Coe, J. A., Staley, D. M., Wasklewicz, T. A., & Tucker, G. E. (2010). Evolution of a natural debris flow: In situ measurements of flow dynamics, video imagery, and terrestrial laser scanning. *Geology*, 38(8), 735–738. <https://doi.org/10.1130/G30928.1>
- McCoy, S. W., Kean, J. W., Coe, J. A., Tucker, G., Staley, D. M., & Wasklewicz, T. (2012). Sediment entrainment by debris flows: In situ measurements from the headwaters of a steep catchment. *Journal of Geophysical Research*, 117(F3). <https://doi.org/10.1029/2011JF002278>
- McCoy, S. W., Tucker, G. E., Kean, J. W., & Coe, J. A. (2013). Field measurement of basal forces generated by erosive debris flows. *Journal of Geophysical Research: Earth Surface*, 118(2), 589–602. <https://doi.org/10.1002/jgrf.20041>
- Middleton, G. V., & Hampton, M. A. (1973). Sediment gravity flows: Mechanics of flow and deposition. *Pacific Section SEPM*.
- MiDi, G. (2004). On dense granular flows. *The European Physical Journal E*, 14(4), 341–365. <https://doi.org/10.1140/epje/i2003-10153-0>
- Mulder, T., & Alexander, J. (2001). The physical character of subaqueous sedimentary density flows and their deposits. *Sedimentology*, 48(2), 269–299. <https://doi.org/10.1046/j.1365-3091.2001.00360.x>

- Munson, B. R., Okiishi, T. H., Huebsch, W. W., & Rothmayer, A. P. (2013). *Fluid mechanics*. Wiley Singapore.
- Ni, H., Zheng, W., Song, Z., & Xu, W. (2014). Catastrophic debris flows triggered by a 4 July 2013 rainfall in Shimian, SW China: Formation mechanism, disaster characteristics and the lessons learned. *Landslides*, *11*(5), 909–921. <https://doi.org/10.1007/s10346-014-0514-9>
- Nordin, C. F. (1963). *A preliminary study of sediment transport parameters: Rio Puerco near Bernardo, New Mexico* (Vol. 462). US Government Printing Office.
- Okano, K., Suwa, H., & Kanno, T. (2012). Characterization of debris flows by rainstorm condition at a torrent on the Mount Yakedake volcano, Japan. *Geomorphology*, *136*(1), 88–94. <https://doi.org/10.1016/j.geomorph.2011.04.006>
- Parker, G. (1979). Hydraulic geometry of active gravel rivers. *Journal of the Hydraulics Division*, *105*(9), 1185–1201. <https://doi.org/10.1061/jyceaj.0005275>
- Parker, G., Wilcock, P. R., Paola, C., Dietrich, W. E., & Pitlick, J. (2007). Physical basis for quasi-universal relations describing bankfull hydraulic geometry of single-thread gravel bed rivers. *Journal of Geophysical Research*, *112*(F4), F04005. <https://doi.org/10.1029/2006JF000549>
- Pierson, T. C. (1980). Erosion and deposition by debris flows at Mt. Thomas, North Canterbury, New Zealand. *Earth Surface Processes*, *5*(3), 227–247. <https://doi.org/10.1002/esp.3760050302>
- Pierson, T. C. (1985). Initiation and flow behavior of the 1980 Pine Creek and Muddy River lahars, Mount St. Helens, Washington. *Geological Society of America Bulletin*, *96*(8), 1056–1069. [https://doi.org/10.1130/0016-7606\(1985\)96<1056:IAFBOT>2.0.CO;2](https://doi.org/10.1130/0016-7606(1985)96<1056:IAFBOT>2.0.CO;2)
- Pierson, T. C., Costa, J. E., & Vancouver, W. (1987). A rheologic classification of subaerial sediment-water flows. Debris flows/avalanches: Process, recognition, and mitigation. *Reviews in Engineering Geology*, *7*, 1–12. <https://doi.org/10.1130/REG7-p1>
- Pierson, T. C., Janda, R. J., Thouret, J.-C., & Borrero, C. A. (1990). Perturbation and melting of snow and ice by the 13 November 1985 eruption of Nevado del Ruiz, Colombia, and consequent mobilization, flow and deposition of lahars. *Journal of Volcanology and Geothermal Research*, *41*(1–4), 17–66. [https://doi.org/10.1016/0377-0273\(90\)90082-Q](https://doi.org/10.1016/0377-0273(90)90082-Q)
- Pierson, T. C., & Scott, K. M. (1985). Downstream dilution of a lahar: Transition from debris flow to hyperconcentrated streamflow. *Water Resources Research*, *21*(10), 1511–1524. <https://doi.org/10.1029/WR021i010p01511>
- Qi, P., & Han, Q. (1991). Resistance characteristics of the hyperconcentration flow on the Yellow River and its calculation (in Chinese). *Yellow River* (pp. 16–22).
- Qi, P., Ru, Y., Zhang, H., & Sun, Z. (1995). The sediment transport capacity issues in Yellow River downstream of Aishan station (in Chinese). *Yellow River*. (pp. 6–11).
- Qi, P., Yu, X., Sun, Z., & Qi, H. (2008). Efficient sediment transport theory of the hyperconcentrated flow in the lower Yellow River (in Chinese). *Journal of Sediment Research*, 74–80.
- Raymond, C. A., McGuire, L. A., Youberg, A. M., Staley, D. M., & Kean, J. W. (2020). Thresholds for post-wildfire debris flows: Insights from the Pinal Fire, Arizona, USA. *Earth Surface Processes and Landforms*, *45*(6), 1349–1360. <https://doi.org/10.1002/esp.4805>
- Reynolds, O. (1883). An experimental investigation of the circumstances which determine whether the motion of water shall be direct or sinuous, and of the law of resistance in parallel channels. *Philosophical Transactions of the Royal Society of London*, 935–982.
- Rouse, H. (1937). Modern conceptions of the mechanics of fluid turbulence. *Transactions of the American Society of Civil Engineers*, *102*(1), 463–505. <https://doi.org/10.1061/taceat.0004872>
- Santos, R., & Duarte, R. M. (2006). Topographic signature of debris flow dominated channels: Implications for hazard assessment. *WIT Transactions on Ecology and the Environment*, *90*. <https://doi.org/10.2495/DEB060291>
- Savage, S. B. (1984). The mechanics of rapid granular flows. In *Advances in applied mechanics* (Vol. 24, pp. 289–366). Elsevier. [https://doi.org/10.1016/S0065-2156\(08\)70047-4](https://doi.org/10.1016/S0065-2156(08)70047-4)
- Savage, S. B., & Hutter, K. (1989). The motion of a finite mass of granular material down a rough incline. *Journal of Fluid Mechanics*, *199*, 177–215. <https://doi.org/10.1017/S0022112089000340>
- Schaefer, J. T. (1990). The critical success index as an indicator of warning skill. *Weather and Forecasting*, *5*(4), 570–575. [https://doi.org/10.1175/1520-0434\(1990\)005<0570:TCSIAA>2.0.CO;2](https://doi.org/10.1175/1520-0434(1990)005<0570:TCSIAA>2.0.CO;2)
- Seegerstrom, K. K., Williams, H., Wilcox, R. E., Foshag, W., & Gonzales, J. R. (1956). *Geologic investigations in the Parícutin area, Mexico*. US Government Printing Office.
- Smola, A. J., & Schölkopf, B. (2004). A tutorial on support vector regression. *Statistics and Computing*, *14*(3), 199–222. <https://doi.org/10.1023/B:STCO.0000035301.49549.88>
- Staley, D. M., Kean, J. W., Cannon, S. H., Schmidt, K. M., & Laber, J. L. (2013). Objective definition of rainfall intensity–duration thresholds for the initiation of post-fire debris flows in southern California. *Landslides*, *10*(5), 547–562. <https://doi.org/10.1007/s10346-012-0341-9>
- Stock, J. D., & Dietrich, W. E. (2006). Erosion of steepland valleys by debris flows. *Geological Society of America Bulletin*, *118*(9–10), 1125–1148. <https://doi.org/10.1130/B25902.1>
- Stock, J. D., Montgomery, D. R., Collins, B. D., Dietrich, W. E., & Sklar, L. (2005). Field measurements of incision rates following bedrock exposure: Implications for process controls on the long profiles of valleys cut by rivers and debris flows. *Geological Society of America Bulletin*, *117*(1–2), 174–194. <https://doi.org/10.1130/B25560.1>
- Suwa, H., Okano, K., & Kanno, T. (2009). Behavior of debris flows monitored on test slopes of Kamikamihorizawa Creek, Mount Yakedake, Japan. *International Journal of Erosion Control Engineering*, *2*(2), 33–45. <https://doi.org/10.13101/ijeece.2.33>
- Swets, J. A. (1988). Measuring the accuracy of diagnostic systems. *Science*, *240*(4857), 1285–1293. <https://doi.org/10.1126/science.3287615>
- Takahashi, T., & Das, D. K. (2014). *Debris flow: Mechanics, prediction and countermeasures*. CRC Press.
- Tang, C., Li, W., Ding, J., & Huang, X. (2011). Field investigation and research on giant debris flow on August 14, 2010 in Yingxiu Town, epicenter of Wenchuan earthquake (in Chinese). *Earth Science - Journal of China University of Geosciences*, 172–180.
- Tang, H., McGuire, L. A., Rengers, F. K., Kean, J. W., Staley, D. M., & Smith, J. B. (2019a). Developing and testing physically based triggering thresholds for runoff-generated debris flows. *Geophysical Research Letters*, *46*(15), 8830–8839. <https://doi.org/10.1029/2019GL083623>
- Tang, H., McGuire, L. A., Rengers, F. K., Kean, J. W., Staley, D. M., & Smith, J. B. (2019b). Evolution of debris-flow initiation mechanisms and sediment sources during a sequence of post wildfire rainstorms. *Journal of Geophysical Research: Earth Surface*, *124*(6), 1572–1595. <https://doi.org/10.1029/2018JF004837>
- Thouret, J.-C., Antoine, S., Magill, C., & Ollier, C. (2020). Lahars and debris flows: Characteristics and impacts. *Earth-Science Reviews*, *201*, 103003. <https://doi.org/10.1016/j.earscirev.2019.103003>
- Vallance, J. W., & Iverson, R. M. (2015). Lahars and their deposits. In *The encyclopedia of volcanoes* (pp. 649–664). Elsevier.
- Vapnik, V. (1964). A note on a class of perceptrons. *Automation and Remote Control*.
- Visa, S., Ramsay, B., Ralescu, A. L., & Van Der Knaap, E. (2011). Confusion matrix-based feature selection. *MAICS*, *710*(1), 120–127.
- Wainwright, J., Parsons, A. J., Cooper, J. R., Gao, P., Gillies, J. A., Mao, L., et al. (2015). The concept of transport capacity in geomorphology. *Reviews of Geophysics*, *53*(4), 1155–1202. <https://doi.org/10.1002/2014RG000474>



- Wendeler, C., Volkwein, A., Roth, A., Denk, M., & Wartmann, S. (2007). Field measurements and numerical modelling of flexible debris flow barriers. In *Debris-flow hazards mitigation: Mechanics, prediction, and assessment* (pp. 681–687). Millpress.
- Wilford, D., Sakals, M., Innes, J., Sidle, R., & Bergerud, W. (2004). Recognition of debris flow, debris flood and flood hazard through watershed morphometrics. *Landslides*, 1(1), 61–66. <https://doi.org/10.1007/s10346-003-0002-0>
- Williams, G. P., & Rosgen, D. L. (1989). *Measured total sediment loads (suspended loads and bedloads) for 93 United States streams*. US Geological Survey Washington.
- Yu, B., Yang, Y., Su, Y., Huang, W., & Wang, G. (2010). Research on the giant debris flow hazards in Zhouqu County, Gansu province on august 7, 2010. (in Chinese). *Journal of Engineering Geology*, 18(4), 437–444.
- Zhou, G. G. D., & Ng, C. W. W. (2010). Dimensional analysis of natural debris flows. *Canadian Geotechnical Journal*, 47(7), 719–729. <https://doi.org/10.1139/T09-134>